Supplemental Material (SM): Crystal Field Induced Defect Compensation in Gd-Doped $PbTiO_3$ Preserving Ferroelectricity and f–Electron Magnetism with Finite-Temperature Multifunctionality

Leila Mollabashi,[1] S. Jalali-Asadabadi,[1,*] Shahrbano Rahimi,[1] Czesław Rudowicz,[2] and Muhammed Acikgoz[3]

[1] *Department of Physics, Faculty of Physics, University of Isfahan (UI), Hezar Jerib Avenue, Isfahan 81746-73441, Iran*
[2] *Faculty of Chemistry, A. Mickiewicz University (AMU), 61-614 Poznań, Poland*
[3] *Department of Science, The State University of New York (SUNY) Maritime College, New York 10465, USA*

This Supplemental Material (SM) supports the main article entitled *"Crystal Field Induced Defect Compensation in Gd-Doped $PbTiO_3$ Preserving Ferroelectricity and f–Electron Magnetism with Finite-Temperature Multifunctionality"* by furnishing an extensive theoretical and computational foundation for the reported findings. Given the intricate coupling of magnetic and ferroelectric degrees of freedom in Gd-doped $PbTiO_3$, especially in the presence of charge-compensating defects and symmetry-reducing site substitutions, this SM offers a systematic exposition of the advanced methods employed to elucidate the origins of room-temperature multiferroicity. We detail two complementary crystal field modeling strategies—hybrid DFT+CFT and semi-empirical SPM+CFT—used to extract symmetry-resolved crystal field parameters and magnetic anisotropy tensors for Gd^{3+} ions under tetragonal and orthorhombic ligand environments. The temperature-dependent magnetic susceptibility is further analyzed via Zeeman and Van Vleck tensor regression, setting the stage for paramagnetic response modeling up to room temperature. Spontaneous polarization is computed using Berry phase formalism, highlighting how defect-assisted lattice distortions modulate ferroelectricity. Electronic and optical band gaps are rigorously evaluated through TB-mBJ and JTSKTB-mBJ schemes, supported by Tauc analysis of the dielectric function. Additionally, a topological analysis of all-electron charge density via QTAIM quantifies charge transfer, oxidation states, and defect-driven redistribution. Comprehensive details of the DFT protocols—including supercell design, Hubbard U parameterization, spin-polarized ground state sampling, and defect energetics—are presented to ensure reproducibility and to enable future extensions. Together, these methodologies reinforce and validate the mechanisms proposed in the main article, linking site-selective Gd doping, defect compensation, and local symmetry breaking to the stabilization of multiferroicity at elevated temperatures.

SMI. INTRODUCTION

The emergence of multiferroicity in lanthanide-doped perovskite oxides has galvanized interest in the interplay between lattice, spin, charge, and orbital degrees of freedom—particularly in systems where defect engineering and site-specific doping act as levers for tuning functionalities. Among these, Gd-doped $PbTiO_3$ (PTO) represents a prototypical platform, capable of simultaneously supporting long-range ferroelectric order and localized magnetic moments under appropriate symmetry and charge-compensation conditions. The main article demonstrates that judicious control of Gd site occupancy and compensating vacancy type can stabilize room-temperature multiferroic behavior in PTO, but such conclusions rest on a complex foundation of intertwined theoretical, numerical, and symmetry-driven insights.

This Supplemental Material is designed to unravel those layers and provide a rigorous methodological blueprint for the computational protocols and physical interpretations presented in the main manuscript. It offers a comprehensive exposition of the theoretical tools used to probe the structural, magnetic, dielectric, and electronic properties of pristine and Gd-doped PTO. Particular focus is given to the hybrid crystal field modeling schemes—DFT+CFT and SPM+CFT—that extract symmetry-resolved crystal field parameters for Gd^{3+} ions under both tetragonal and orthorhombic distortions. These parameters inform the calculation of Zeeman and Van Vleck tensors, which in turn reveal the temperature- and orientation-dependent magnetic susceptibility—an essential descriptor of paramagnetic response.

In parallel, we outline the application of Berry phase theory for computing spontaneous electric polarization across stoichiometric and defect-laden structures, showing how local lattice asymmetries induced by Gd substitution reinforce ferroelectricity. Band gap evaluations are carried out via both semi-local (PBE+U) and meta-GGA (TB-mBJ and JTSKTB-mBJ) formalisms, corroborated by Tauc-based optical absorption analyses. The semiconducting nature of charge-neutralized Gd-PTO is thus established in a cross-validated fashion. Furthermore, QTAIM-based topological analyses of electron density elucidate the redistribution of charge around dopants and vacancies, enabling robust inference of valence states, bonding, and covalency.

This document also contains extensive computational details on supercell design, Brillouin zone sampling, spin configurations, defect formation energies, and susceptibility modeling. Together, these technical foundations not only ensure methodological transparency and reproducibility but also pave the way for generalizing the framework to other complex oxide systems. In doing so, this Supplemental Material bridges the microscopic physics and macroscopic observables of Gd-doped PTO, underpinning the central thesis of room-temperature multiferroicity via site selectivity and

* Corresponding author: saeid.jalali.asadabadi@gmail.com, sjalali@sci.ui.ac.ir

electronic stabilization.

SMII. FUNDAMENTAL THEORETICAL METHODOLOGIES

A. Crystal-Field Hamiltonian for Gd^{3+}

The electronic states of Gd^{3+} in $PbTiO_3$-based compounds are described by the effective Hamiltonian

$$\hat{H} = \hat{H}_{\mathrm{A}} + \hat{H}_{\mathrm{CF}} + \hat{H}_{\mathrm{ex}} + \tilde{H}_{\mathrm{Z}}, \tag{SM1}$$

where $\hat{H}_{\mathrm{A}}$ is the free-ion Hamiltonian [1], $\hat{H}_{\mathrm{CF}}$ the crystal-field (CF) term, $\hat{H}_{\mathrm{ex}}$ the exchange interaction, and $\tilde{H}_{\mathrm{Z}}$ the effective Zeeman interaction [2].

The CF Hamiltonian is written in Wybourne notation [3–5] as

$$\hat{H}_{\mathrm{CF}} = \sum_{k,q} B_{kq} \hat{C}_q^{(k)}, \tag{SM2}$$

with spherical tensor operators

$$\hat{C}_q^{(k)} = \sqrt{\frac{4\pi}{2k+1}}\, \hat{Y}_q^k. \tag{SM3}$$

The allowed CFPs B_{kq} are fixed by the local point symmetry of the Gd^{3+} site.

For tetragonal C_{4v} symmetry, the CF Hamiltonian reads

$$\begin{aligned}\hat{H}_{\mathrm{CF}} = {} & B_{20}\hat{C}_0^{(2)} + B_{40}\hat{C}_0^{(4)} + B_{44}(\hat{C}_4^{(4)} + \hat{C}_{-4}^{(4)}) \\ & + B_{60}\hat{C}_0^{(6)} + B_{64}(\hat{C}_4^{(6)} + \hat{C}_{-4}^{(6)}),\end{aligned} \tag{SM4}$$

as obtained from Eq. (SM2) for real CFPs [6].

In Pb-vacancy–stabilized configurations, the symmetry lowers to C_{2v}, activating additional CFPs:

$$\begin{aligned}\hat{H}_{\mathrm{CF}} = {} & B_{20}\hat{C}_0^{(2)} + B_{22}(\hat{C}_2^{(2)} + \hat{C}_{-2}^{(2)}) + B_{40}\hat{C}_0^{(4)} \\ & + B_{42}(\hat{C}_2^{(4)} + \hat{C}_{-2}^{(4)}) + B_{44}(\hat{C}_4^{(4)} + \hat{C}_{-4}^{(4)}) \\ & + B_{60}\hat{C}_0^{(6)} + B_{62}(\hat{C}_2^{(6)} + \hat{C}_{-2}^{(6)}) + B_{64}(\hat{C}_4^{(6)} + \hat{C}_{-4}^{(6)}).\end{aligned} \tag{SM5}$$

Crystal-field parameters were obtained using two complementary schemes: DFT+CFT (Wannier-projected $4f$ Hamiltonians) and SPM+CFT (geometry-based ligand contributions). Implementation details are provided in the subsequent SM sections.

1. *CFPs Determination by Hybrid DFT+CFT Approach*

Crystal-field parameters (CFPs) of Gd^{3+} were obtained using the parameter-free DFT+CFT approach [6–9], which combines first-principles electronic structure calculations with crystal-field theory via projection onto the localized $4f$ manifold.

Calculations start from a non-spin-polarized open-core DFT treatment of the Gd $4f$ shell [10–12], suppressing self-interaction errors while preserving strong $4f$ localization. Hybridization between Gd $4f$ and O $2p/2s$ states is subsequently introduced through an energy shift parameter Δ [6, 7, 9]. A non-self-consistent calculation is then performed with the $4f$ states promoted to the valence, yielding the local $4f$ Hamiltonian $\hat{H}_{4f}$.

Bloch states in the $4f$ energy window are projected onto maximally localized Wannier functions using WIEN2WANNIER [13] and WANNIER90 [14–17], producing a 7×7 on-site Hamiltonian. The crystal-field Hamiltonian is obtained from its traceless part [7]:

$$\hat{H}_{\mathrm{CF}} = \hat{H}_{4f} - E_{\mathrm{avg}}\hat{I}, \tag{SM6}$$

with $E_{\mathrm{avg}} = \mathrm{Tr}(\hat{H}_{4f})/7$.

The CFPs B_{kq} are extracted by expanding $\hat{H}_{\mathrm{CF}}$ in Wybourne-normalized spherical tensor operators $\hat{C}_q^{(k)}$ [Eqs. (SM2)–(SM3)], with $k_{\max} = 6$ for f electrons. This procedure preserves site symmetry and explicitly incorporates covalency and hybridization effects, providing a reliable microscopic basis for analyzing magnetic anisotropy, Zeeman splitting, and spectroscopic fine structure in Gd-doped $PbTiO_3$.

2. *CFPs Determination by Hybrid SPM+CFT Approach*

Crystal-field parameters were also evaluated using the semi-empirical superposition model (SPM) combined with crystal-field theory [18–21]. In SPM, the ligand field at the central ion is expressed as a sum of individual ligand contributions, allowing a transparent separation of geometric and intrinsic interaction effects. This makes the approach particularly suitable for low-symmetry and defect-containing environments [22].

In extended Stevens notation, the CFPs are written as [23–26]:

$$b_k^q = \sum_{i=1}^{n} \bar{b}_k(R_i)\, K_k^q(\theta_i, \phi_i), \tag{SM7}$$

where (R_i, θ_i, ϕ_i) denote the ligand coordinates and K_k^q are geometrical coordination factors. The intrinsic parameters follow a power-law distance dependence,

$$\bar{b}_k(R_i) = \bar{b}_k(R_0)\left(\frac{R_0}{R_i}\right)^{t_k}, \tag{SM8}$$

with reference distance R_0 and rank-dependent exponent t_k.

Equivalently, in Wybourne notation the CFPs read [4, 22, 27]:

$$B_{kq} = \sum_i \bar{A}_k \left(\frac{R_0}{R_i}\right)^{t_k} K_{kq}(\theta_i, \phi_i), \tag{SM9}$$

which is used throughout this work for consistency with the DFT+CFT analysis. For low-symmetry sites, the Stevens formalism guarantees real CFPs, while the Wybourne parameters are related by standard transformations [22].

The key advantage of SPM is its parsimony: instead of fitting a full set of B_{kq} parameters, only a small number of physically meaningful quantities ($\bar{A}_k$, t_k, R_0) are required, enhancing transferability across structurally related systems [22, 28, 29]. This feature is particularly valuable for vacancy-induced symmetry lowering, such as the $C_{4v} \rightarrow C_{2v}$ reduction caused by Pb vacancies in $PbTiO_3$.

In this study, SPM was applied using DFT-relaxed geometries for Gd^{3+} at Pb and Ti sites. Coordination factors K_{kq} for C_{4v} and C_{2v} symmetries were taken from tabulated expressions [22]. To assess robustness, three parameter sets were tested: SPM(a) with nominal $\bar{A}_k$ values [30], SPM($b^{\pm}$) varying $\bar{A}_k$ by ±20%, and SPM($c^{\pm}$) varying t_k by ±20%. The resulting CFP trends are compared directly with the DFT+CFT results in Sec. II F, see Tables CI and CII in the main article.

B. Zeeman Splitting and Van Vleck Susceptibility of the Ground Multiplet

Gd^{3+} has a half-filled $4f^7$ shell with $L = 0$, resulting in $S = J = 7/2$ and a ${}^8S_{7/2}$ ground-state multiplet; the first excited multiplet ${}^6P_{7/2}$ ($L = 1$, $S = 5/2$) lies at higher energy. In the crystalline environment, crystal fields and spin–orbit coupling split each $J = 7/2$ multiplet into symmetry-dependent Kramers doublets. Under tetragonal C'_{4v} symmetry, relevant for $Pb_{0.875}Gd_{0.125}TiO_3$ and $PbTi_{0.875}Gd_{0.125}O_{3-\delta}$, the splitting follows $2\Gamma_6 + 2\Gamma_7$, while symmetry lowering to C'_{2v} (Pb-vacancy systems) yields four Γ_5 doublets [31].

The field-dependent energies of the ith Kramers doublet are modeled as [9]

$$\varepsilon_i(\mathbf{B}) = \varepsilon_i(0) \pm \tfrac{1}{2}\mu_B\, \mathbf{B}\cdot\mathbf{g}_i(\hat{\mathbf{n}}) - \tfrac{1}{2}\mathbf{B}\cdot\boldsymbol{\chi}_i^{\mathrm{vV}}\cdot\mathbf{B}, \tag{SM10}$$

where $\mathbf{g}_i$ is the effective Zeeman tensor, $\boldsymbol{\chi}_i^{\mathrm{vV}}$ the Van Vleck susceptibility tensor, and $\hat{\mathbf{n}} = \mathbf{B}/|\mathbf{B}|$. The zero-field energies $\varepsilon_i(0)$ include crystal-field and exchange contributions.

The tensors $\mathbf{g}_i$ and $\boldsymbol{\chi}_i^{\mathrm{vV}}$ were extracted by quadratic regression of field-induced level splittings obtained from diagonalization of the crystal-field Hamiltonian using both DFT+CFT and SPM+CFT CFPs. Formal definitions of $\mathbf{g}_i$ are given in Eqs. (5)–(11) of Ref. [9].

The magnetic moment of the ith state along direction ν is

$$m_{i,\nu} = -\frac{d\varepsilon_{i,\nu}}{dB_\nu}, \tag{SM11}$$

and the thermally averaged magnetization follows Boltzmann statistics,

$$M_\nu(T) = \frac{\sum_i m_{i,\nu} e^{-\varepsilon_{i,\nu}/k_BT}}{\sum_i e^{-\varepsilon_{i,\nu}/k_BT}}, \tag{SM12}$$

from which the susceptibility is obtained as

$$\chi_\nu(T) = \frac{\partial M_\nu}{\partial B_\nu}. \tag{SM13}$$

This framework yields anisotropic susceptibilities $\chi_\parallel(T)$ and $\chi_\perp(T)$, directly linking symmetry-controlled crystal-field splittings to temperature-dependent magnetic response. For clarity, the two computational protocols employed are denoted as (i) DFT+CFT+Δ+Zeem.+Reg. and (ii) SPM+CFT+Zeem.+Reg., following Ref. [9].

C. Electronic and Optical Band Gaps

Standard DFT underestimates band gaps due to the lack of derivative discontinuity in semi-local exchange–correlation functionals [32–37]. To overcome this limitation, electronic band gaps were evaluated using the Tran–Blaha modified Becke–Johnson (TB-mBJ) exchange potential [32], which introduces a semi-local correction via a system-dependent scaling factor

$$c = A + B\sqrt{\frac{1}{\Omega}\int_\Omega \frac{|\nabla\rho(\mathbf{r})|}{\rho(\mathbf{r})}\,d\mathbf{r}}, \tag{SM14}$$

with $A = -0.012$ and $B = 1.023\sqrt{\mathrm{Bohr}}$ [38]. Here, $\rho(\mathbf{r})$ is the electron density and Ω the unit-cell volume. For correlated oxides, the generalized JTSKTB-mBJ scheme [39] was additionally employed, using $c = A + B\overline{g}^{\,e}$ with $A = 0.4$, $B = 1.0\sqrt{\mathrm{Bohr}}$, and $e = 0.5$.

Optical properties were obtained from the complex dielectric function $\varepsilon(\omega) = \varepsilon_1(\omega) + i\varepsilon_2(\omega)$ calculated within the random-phase approximation (RPA). The imaginary part is given by

$$\Im[\varepsilon_{\alpha\alpha'}(\omega)] = \left(\frac{e^2\Omega}{2\pi\hbar m^2\omega^2}\right)\sum_{cv}\int d\mathbf{k}\,\langle c\mathbf{k}|p_\alpha|v\mathbf{k}\rangle\langle v\mathbf{k}|p_{\alpha'}|c\mathbf{k}\rangle \times f_{v\mathbf{k}}(1-f_{c\mathbf{k}})\delta(E_{c\mathbf{k}} - E_{v\mathbf{k}} - \hbar\omega), \tag{SM15}$$

while $\Re[\varepsilon(\omega)]$ follows from the Kramers–Kronig relation,

$$\Re[\varepsilon(\omega)] = 1 + \frac{2}{\pi}\mathcal{P}\int_0^\infty \frac{\omega'\Im[\varepsilon(\omega')]}{\omega'^2 - \omega^2}\,d\omega'. \tag{SM16}$$

The absorption coefficient was computed as

$$\alpha(\omega) = \frac{2\omega\kappa(\omega)}{c}, \tag{SM17}$$

where $\kappa(\omega)$ is the extinction coefficient derived from the complex refractive index. The optical band gap E_g^{opt} was extracted using the Tauc relation [40],

$$(\alpha\hbar\omega)^{1/\gamma} = B(\hbar\omega - E_g^{\mathrm{opt}}), \tag{SM18}$$

with $\gamma = 1/2$ and 2 for direct and indirect allowed transitions, respectively.

This combined TB-mBJ/JTSKTB-mBJ and RPA+Tauc framework provides consistent electronic and optical band gaps for Gd-doped $PbTiO_3$, enabling direct comparison with experiment. Further methodological details are given in Ref. [41].

D. Topological Analysis of Charge Density via QTAIM

Charge redistribution in pristine and Gd-doped $PbTiO_3$ was analyzed using the Quantum Theory of Atoms in Molecules (QTAIM) [42, 43], which partitions the electron density $\rho(\mathbf{r})$ into atomic basins bounded by zero-flux surfaces,

$$\nabla\rho(\mathbf{r}) \cdot \mathbf{n}(\mathbf{r}) = 0, \tag{SM19}$$

where $\mathbf{n}(\mathbf{r})$ is the surface normal. The electron population associated with each atom is given by the Bader charge

$$Q_{\text{Bader}} = \int_{\Omega} \rho(\mathbf{r})\, d\mathbf{r}, \tag{SM20}$$

providing a quantitative measure of charge transfer and bond ionicity.

All-electron charge densities were obtained from FP-APW+lo calculations [44, 45] using WIEN2k [46–48] and analyzed with Critic2 [49, 50]. This approach was applied to stoichiometric, Gd-substituted, and vacancy-stabilized $PbTiO_3$ configurations. The resulting Bader electron charges reveal systematic charge redistribution induced by aliovalent Gd substitution and intrinsic defects, directly correlating with modifications of Ti–O bond ionicity, Pb lone-pair activity, and local electronic environments discussed in the main text.

Further methodological background and applications of QTAIM to complex oxides are given in Refs. [51, 52].

E. Spontaneous Polarization from Berry Phase Theory

Spontaneous polarization of pristine and Gd-doped $PbTiO_3$ was computed using the modern Berry-phase theory of polarization within DFT+U [53–59]. For a structural phase λ, the total polarization reads [41, 60]

$$\begin{aligned}\mathbf{P}^{(\lambda)} = &\frac{e}{\Omega^{(\lambda)}} \sum_{s=1}^{N} Z_s^{\text{ion}(\lambda)} \mathbf{r}_s^{(\lambda)} \\ &+ \frac{2e}{(2\pi)^3} \sum_{n=1}^{M} \int_{1\text{BZ}^{(\lambda)}} d\mathbf{k}\, \langle u_{n\mathbf{k}}^{(\lambda)} | -i\nabla_{\mathbf{k}} | u_{n\mathbf{k}}^{(\lambda)} \rangle,\end{aligned} \tag{SM21}$$

where the first term is the ionic contribution and the second is the electronic Berry phase term.

Expressed geometrically, the polarization component along lattice vector $R_\mu^{(\lambda)}$ is

$$P_\mu^{(\lambda)} = \frac{e}{2\pi} \frac{\varphi_\mu^{(\lambda)}}{\Omega^{(\lambda)}} R_\mu^{(\lambda)}, \tag{SM22}$$

with $\varphi_\mu^{(\lambda)}$ the Berry phase.

The spontaneous polarization is obtained from the difference between the low- and high-symmetry phases,

$$\mathbf{P}_s = \mathbf{P}^{(2)} - \mathbf{P}^{(1)}. \tag{SM23}$$

This gauge-invariant formalism accurately captures both ionic displacements and electronic rearrangements induced by aliovalent Gd substitution and compensating defects. Further computational details are given in Refs. [41, 60] and the Supplemental Material of Ref. [60].

F. Choice and robustness of the on-site Coulomb interaction parameters

The on-site Coulomb interaction was treated within the Dudarev formalism, using the effective parameter $U_{\text{eff}} = U - J$. The values adopted in this work, $U_{\text{eff}}^{\text{Gd}} = 4.35$ eV for Gd $4f$ states and $U_{\text{eff}}^{\text{Ti}} = 3.94$ eV for Ti $3d$ states, were not treated as fitting parameters but were taken from well-established literature for closely related rare-earth and transition-metal oxide systems.

For Gd $4f$ states, the choice $U_{\text{eff}}^{\text{Gd}} = 4.35$ eV is motivated by the comprehensive first-principles analysis of Bjaalie *et al.* [67], who determined the Mott–Hubbard gap in $GdTiO_3$ and demonstrated that values in the range $U_{\text{eff}}^{\text{Gd}} \approx 4$–$5$ eV correctly reproduce the localization, energetic position, and magnetic character of Gd $4f$ states. This range has since become standard in DFT+U studies of Gd-containing perovskite and oxide materials and provides a physically sound description of strongly localized $4f$ electrons.

For Ti $3d$ states, $U_{\text{eff}}^{\text{Ti}} = 3.94$ eV is consistent with prior studies of $PbTiO_3$ and related titanates, including the work of Shimada *et al.* [68], where comparable U_{eff} values were employed to capture electron-correlation effects associated with Ti–O bonding, defect-induced charge redistribution, and local electronic reconstruction in ferroelectric environments.

To explicitly assess the sensitivity of our results to the choice of U_{eff}, we examined the evolution of the electronic structure as a function of $U_{\text{eff}}^{\text{Ti}}$ over a wide physically relevant range (1–9 eV), while keeping $U_{\text{eff}}^{\text{Gd}}$ fixed at its literature value. As summarized in Table SM1, increasing $U_{\text{eff}}^{\text{Ti}}$ leads to a systematic and monotonic widening of the band gap in pristine $PbTiO_3$, as expected for correlated d states, but does not alter the qualitative nature of the electronic structure (indirect gap) nor the insulating character of the system. Crucially, for Gd-doped and vacancy-stabilized configurations, the reopening of the band gap upon charge compensation, the relative energetic position of the Gd $4f$ manifold, and the total magnetic moment per Gd atom remain robust across this entire range of $U_{\text{eff}}^{\text{Ti}}$ values.

Likewise, systematic benchmarking of the effective Hubbard parameter for Gd $4f$ states in Gd-containing systems—including our recent study of $GdAl_2$ summarized in Table I of Ref. [69]—demonstrates that moderate variations of $U_{\text{eff}}^{\text{Gd}}$ within the physically relevant range ($\sim$ 4–6 eV) primarily affect quantitative details, such as equilibrium lattice constants and elastic moduli, while leaving the qualitative electronic and magnetic characteristics unchanged. In particular, the localized nature of the Gd $4f$ states, the magnitude of the magnetic moment, and the magnetic ground state are robust against reasonable variations of $U_{\text{eff}}^{\text{Gd}}$.

A similar robustness with respect to the Hubbard parameter has been demonstrated in our recent systematic study of correlated oxides and metals (Table SM2 in Supplemental

TABLE SM1. The electronic bangap (E_g^e), type of electronic band gap (Type), direct optical band gap (dir. E_g^{opt}), and indirect optical bandgap (ind. E_g^{opt}) for for the $PbTiO_3$, $Pb_{0.875-\delta}Gd_{0.125}TiO_3$, and $PbTi_{0.875}Gd_{0.125}O_{3-\delta}$. Total magnetic moment per Gd atom (MM). XC, SOC, c, and U_{eff} represent exchange-correlation, spin-orbit coupling, c parameter of various mBJ versions, including TB-mBJ and JTSKTB-mBJ as defined and discussed in Sec. SMII C and Ref. [41], and effective Hubbard parameter of GGA+U, respectively. Results of this work are denoted by *.

Compound	Structure	Scheme	SOC	c	U_{eff}^{Ti} (eV)	U_{eff}^{Gd} (eV)	E_g^e (eV)	Type	$E_{g,\,dir.}^{opt}$ (eV)	$E_{g,\,ind.}^{opt}$ (eV)	MM (μ_B)	Ref.
$PbTiO_3$	Bulk/tetra.	PBE-GGA	Yes	-	-	-	1.78	ind.	3.2	2.5	-	*
		PBE-GGA+U	Yes	-	0.99	-	1.88	ind.	3.4	2.4	-	*
		PBE-GGA+U	Yes	-	2.04	-	1.99	ind.	3.4	2.5	-	*
		PBE-GGA+U	Yes	-	2.99	-	2.06	ind.	3.5	2.5	-	*
		PBE-GGA+U	Yes	-	3.94	-	2.20	ind.	3.5	2.6	-	*
		PBE-GGA+U	Yes	-	5.03	-	2.32	ind.	3.6	2.6	-	*
		PBE-GGA+U	Yes	-	5.99	-	2.42	ind.	3.7	2.6	-	*
		PBE-GGA+U	Yes	-	6.94	-	2.54	ind.	3.8	2.6	-	*
		PBE-GGA+U	Yes	-	8.03	-	2.66	ind.	3.3	2.3	-	*
		PBE-GGA+U	Yes	-	8.98	-	2.70	ind.	2.2	1.0	-	*
		TB-mBJ	Yes	1.38	-	-	2.08	ind.	3.6	3.1	-	*
		JTSKTB-mBJ	Yes	1.80	-	-	2.60	ind.	3.7	3.2	-	*
	Bulk/tetra.	PW91-GGA		-		-	1.56	dir.			-	[61]
	Bulk/cub.	B3PW		-		-				2.87	-	[62]
	Thin film/tetra.	Exp.		-		-			3.45		-	[63]
	Bulk/cub.	DFT-HF hybrid		-		-					-	[63]
	Thin film/tetra.	Exp.		-		-			3.7		-	[64]
	Thin film/tetra.	Exp.		-		-			3.88		-	[65]
	Thin film/cub.	Exp.		-		-			3.67		-	[65]
	nanoparticle/-	Exp.		-		-				2.6	-	[66]
$Pb_{0.875-\delta}Gd_{0.125}TiO_3$	Bulk/tetra.	PBE-GGA+U	Yes	-	-	4.35	1.82	dir.	3.5	2.5	6.93	*
		PBE-GGA+U	Yes	-	3.94	3.35	2.23	dir.	3.7	2.8	6.93	*
		PBE-GGA+U	Yes	-	3.94	4.35	2.23	dir.	3.7	2.8	6.93	*
		PBE-GGA+U	Yes	-	3.94	5.35	2.23	dir.	3.7	2.8	6.93	*
$PbTi_{0.875}Gd_{0.125}O_{3-\delta}$		PBE-GGA+U	Yes	-	-	4.35	1.73	dir.	3.4	2.6	6.85	*
		PBE-GGA+U	Yes	-	3.94	3.35	1.84	dir.	3.7	2.6	6.85	*
		PBE-GGA+U	Yes	-	3.94	4.35	1.84	dir.	3.7	2.6	6.85	*
		PBE-GGA+U	Yes	-	3.94	5.35	1.84	dir.	3.7	2.6	6.85	*

Material of Ref. [60]), where extensive benchmarking over multiple exchange–correlation functionals, magnetic configurations, spin–orbit coupling, and a broad range of U values showed that varying U primarily affects quantitative metrics such as lattice parameters or gap magnitudes, while leaving the qualitative electronic phase (metallic versus insulating) and symmetry-driven trends unchanged. In that work, as here, the inclusion of U shifts energetic thresholds but does not qualitatively alter the underlying physical mechanisms.

We therefore conclude that the central findings of this work—namely, defect-induced charge compensation, stabilization of insulating behavior, preservation of f-electron magnetism, and the resulting crystal-field–controlled magnetic anisotropy—are not artifacts of a specific numerical choice of U, but are robust features of the underlying physics captured within a physically motivated and literature-supported GGA+U framework.

G. Supercell Construction and Brillouin Zone Sampling

To model the Gd-doped $PbTiO_3$ compositions, a $2 \times 2 \times 2$ supercell was employed for $Pb_{1-x}Gd_xTiO_3$ ($Pb_{0.875}Gd_{0.125}TiO_3$), while $2 \times 2 \times 4$ supercells were used for

$Pb_{1-x-\delta}Gd_xTiO_3$ ($Pb_{0.8125}Gd_{0.125}TiO_3$) and $PbTi_{1-x}Gd_xO_{3-\delta}$ ($PbTi_{0.875}Gd_{0.125}O_{2.9375}$). Here, $x = 1/8 = 0.125$ denotes the Gd doping level, corresponding to substitution of one out of eight Pb or Ti atoms by Gd^{3+} in the respective supercells. The vacancy concentration is given by $\delta = 1/16 = 0.0625$, introduced either as a Pb-site vacancy (V_{Pb}) or an oxygen vacancy (V_O) to maintain charge neutrality. Full structural details, including atom indices and symmetry settings, are provided in the ESI of Ref. [70]. Brillouin zone integrations were carried out using Monkhorst-Pack meshes [71] with $5\times5\times5$ and $5\times5\times3$ k-point grids for structural relaxation. For band structure and optical property calculations, denser $9\times9\times8$ and $9\times9\times4$ grids were employed, respectively.

H. Magnetic Configuration Sampling and Spin-Polarized Calculations

As pure $PbTiO_3$ (PTO) is non-magnetic [72], magnetic ordering is not expected in its undoped form. However, upon Gd doping, magnetic behavior becomes plausible, especially in light of prior observations of ferromagnetism in PTO doped with Fe and Gd nanorods [73]. To systematically assess the magnetic character introduced by Gd^{3+} substitution, we performed total energy calculations for non-magnetic (NM), ferromagnetic (FM), and antiferromagnetic (AFM) configurations for all doped compositions. These magnetic configurations were examined for both Pb-site and Ti-site Gd doping, with accompanying Pb or O vacancies. The relative energies of FM and AFM states provided insight into the preferred spin alignment induced by the Gd dopants in the $PbTiO_3$ lattice. The spin-polarized calculations were carried out consistently within the GGA+U framework, as described above, enabling a quantitative evaluation of the magnetic stabilization associated with Gd incorporation.

I. Defect Formation Energy Calculations

To ensure consistency in formation energy calculations, we employed $2\times2\times4$ supercells for all doped configurations, including those without intrinsic vacancies, matching the supercell dimensions used for vacancy-containing structures. The formation energy of a vacancy-type defect, E_f^D, was computed using the relation $E_f^D = E_{\text{Total}}(\text{with Vac.}) - E_{\text{Total}}(\text{without Vac.}) + E_{\text{atom}}(\text{Vac.})$, following the methodology outlined in Ref. [70]. Here, $E_{\text{Total}}(\text{with Vac.})$ and $E_{\text{Total}}(\text{without Vac.})$ refer to the total energies of supercells with and without the vacancy, respectively, while $E_{\text{atom}}(\text{Vac.})$ represents the isolated atomic energy of the removed Pb or O atom, calculated in its respective ground state configuration.

J. Electronic Band Gap Corrections

To address the well-known underestimation of band gaps in standard DFT [32–37], we employed the modified Becke-Johnson (TB-mBJ) exchange potential and its tailored extensions, as systematically reviewed in Ref. [41]. Our calculations incorporated both the original TB-mBJ scheme [32, 33], characterized by the expression $c = \alpha + \beta\sqrt{\overline{g}}$ with $\alpha = -0.012$ and $\beta = 1.023\ \sqrt{\text{Bohr}}$, and the JTSKTB-mBJ variant [39], which generalizes the c parameter as $c = A + B\overline{g}^e$ using $A = 0.4$, $B = 1.0\ \sqrt{\text{Bohr}}$, and $e = 0.5$. The JTSKTB-mBJ parametrization was developed to enhance accuracy in perovskite systems by adjusting the c factor based on their specific electronic environments. In this study, both formulations were applied self-consistently to evaluate their performance on the $PbTiO_3$-based compounds. This dual approach enabled a cross-validation of results and offered a broader perspective on the sensitivity of band gap predictions to exchange potential parametrizations in complex oxide materials.

K. Optical Band Gap Extraction via Tauc Analysis

For the evaluation of optical band gaps, we applied the Tauc method by plotting $(\alpha\hbar\omega)^2$ and $(\alpha\hbar\omega)^{1/2}$ as functions of photon energy, corresponding to direct and indirect transitions, respectively. These plots were generated from the absorption coefficients obtained via the calculated dielectric functions, following the procedure outlined in Sec. SMII C and demonstrated in Ref. [41].

In optical spectroscopy, the Tauc method is widely used to estimate the optical band gap E_g^{opt} of semiconductors and insulators based on the absorption coefficient spectrum. The method is grounded in the relationship expressed in Eq. (SM18). A Tauc plot is created by plotting $(\alpha\hbar\omega)^{1/\gamma}$ on the vertical Y-axis against E on the horizontal axis. The onset of the absorption edge appears as a linear region, and extrapolating this region to the energy axis gives the band gap E_g^{opt}. To accurately estimate E_g^{opt}, a tangent must be drawn to the linear region of the Tauc plot. While this is often done manually by visual inspection, the choice of tangent line is critical and must be made with care. In this work, we present a systematic procedure for selecting the optimal tangent and estimating the optical band gap using the Tauc method. The steps are detailed below and visually summarized in the flowchart shown in Fig. SM1. A valid tangent line: must lie entirely below or on the Tauc curve in the selected region, must touch the curve at exactly one point, and should have the maximum possible slope under these conditions. The procedure begins by selecting a suitable energy interval $[E_{\min}, E_{\max}]$ where the Tauc plot appears approximately linear. Within this interval, all pairs of data points (E_i, Y_i) and (E_j, Y_j) are considered, where Y_j denotes the j-th value of the transformed absorption data, $Y = (\alpha\hbar\omega)^{1/\gamma}$. For each pair, a candidate line is formed:

$$m = \frac{Y_j - Y_i}{E_j - E_i}, \quad c = Y_i - mE_i. \tag{SM24}$$

This line has the form $Y = mE + c$, where $Y = (\alpha\hbar\omega)^{1/\gamma}$. The line is tested against all other points in the interval to ensure

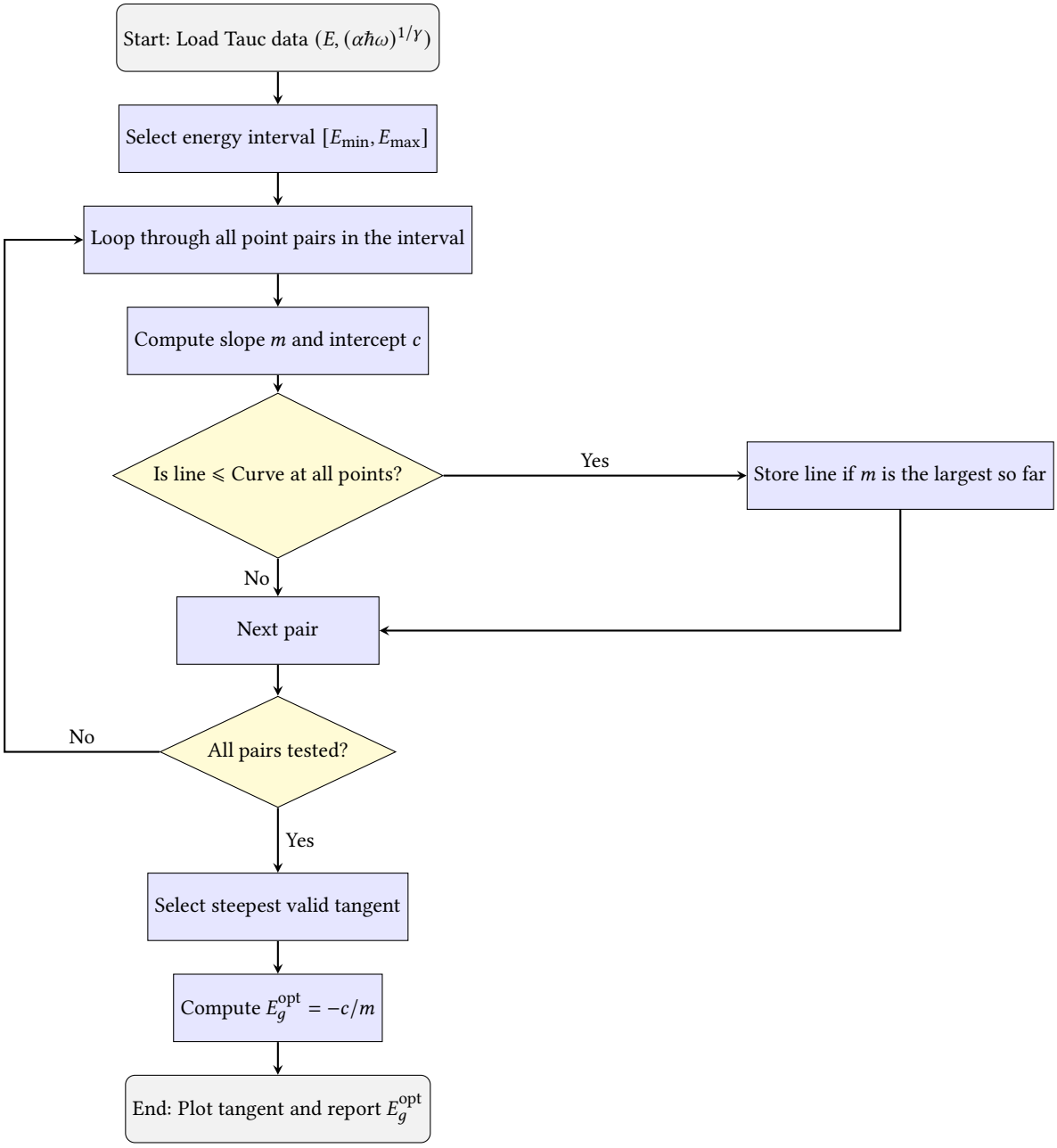

FIG. SM1. **Flowchart illustrating the algorithm used to estimate the optical band gap E_g^{opt} from a Tauc plot.** The process begins with loading the photon energy E and transformed absorption data $(\alpha\hbar\omega)^{1/\gamma}$, where $\gamma = 2$ or $1/2$ depending on whether direct or indirect transitions are considered. A suitable energy interval $[E_{\min}, E_{\max}]$ is then selected where the Tauc curve appears approximately linear. All pairs of data points within this interval are tested to form candidate tangent lines, each defined by its slope m and intercept c. A line is considered valid only if it lies entirely below or on the Tauc curve and touches it at exactly one point. Among all valid lines, the one with the maximum slope is selected as it corresponds to the earliest physically meaningful onset of absorption. The optical band gap is then obtained by extrapolating this line to the energy axis, using $E_g^{\text{opt}} = -c/m$. This approach ensures consistency with the theoretical foundations of the Tauc method and avoids under- or overestimation of the gap due to misaligned tangents.

it lies below or on the curve:

$$mE_k + c \leq Y_k, \quad \text{for all } k. \tag{SM25}$$

If the condition is satisfied, the line is considered a valid tangent. Among all valid lines, the one with the maximum slope m is selected, as this choice is both physically justified and methodologically essential for a reliable estimate of the optical band gap. In the Tauc plot, a steeper tangent reflects a more abrupt rise in the absorption coefficient, characteristic of a well-defined electronic transition at the absorption edge. By selecting the steepest possible line that remains entirely below (or on) the Tauc curve and touches it only once, we en-

sure that the extrapolated intercept corresponds to the earliest physically meaningful onset of optical absorption. Choosing a line with a lower slope, though still valid in the mathematical sense of tangency, would result in an x-axis intercept at a lower energy. This implies that absorption begins at photon energies below those actually supported by the data, thereby underestimating the band gap. Such a choice is inconsistent with the physical behavior of the material, where absorption only becomes appreciable once the photon energy exceeds the gap. Conversely, lines with slopes greater than the maximum valid one would inevitably intersect the curve, violating the physical requirement that no absorption occurs below the band edge. Hence, the tangent with the maximum admissible slope is unique in that it satisfies all physical constraints while capturing the sharpest, earliest linear rise in absorption. This approach not only adheres to the theoretical assumptions of the Tauc model but also mimics the expert judgment traditionally applied in experimental interpretation, now implemented with algorithmic rigor. It thus provides a robust, accurate, and physically consistent determination of E_g^{opt}. The band gap is then determined from the horizontal energy-axis intercept of this tangent line:

$$E_g^{\text{opt}} = -\frac{c}{m}. \tag{SM26}$$

This method guarantees a physically meaningful estimate of the optical band gap. It mimics what a trained analyst might do manually, but with the objectivity and precision of algorithmic computation. By strictly adhering to the criteria of tangency and non-intersection, the resulting E_g aligns with the theoretical assumptions of the Tauc model.

L. Spontaneous Electric Polarization Calculations

To compute the spontaneous electric polarization of the $PbTiO_3$-based compounds under investigation, we utilized the Berry phase formalism within the DFT framework, as implemented the WIEN2k package [46–48]. In practice, we calculated the polarization difference between the low-symmetry (tetragonal) and high-symmetry (cubic) phases of each compound. This difference corresponds to the spontaneous polarization and is given by: $\mathbf{P}_{\text{spontaneous}} = \mathbf{P}_{\text{tetragonal}} - \mathbf{P}_{\text{cubic}}$. The Berry phase calculations accounted for both electronic and ionic contributions to the polarization. The electronic part was obtained by integrating the Berry connection over the occupied valence bands in reciprocal space, while the ionic part was determined from the positions of the nuclei and their respective charges. This methodology provides a robust and accurate means of determining spontaneous polarization in ferroelectric materials, capturing the essential physics associated with structural distortions and electronic rearrangements.

M. Charge Density Analysis

To assess the charge distribution in $Pb_{0.8125}Gd_{0.125}TiO_3$ and $PbTi_{0.875}Gd_{0.125}O_{2.9375}$ compounds, we performed a topological analysis of the all-electron charge densities using the Quantum Theory of Atoms in Molecules (QTAIM) formalism. The charge densities were obtained from DFT calculations using the FP-APW+lo method as implemented in the WIEN2k package [46–48]. The resulting densities were subsequently analyzed with the Critic2 code [49, 50], which partitions space into atomic basins based on zero-flux surfaces in the gradient field of the electron density. Bader electron charges (BECs) were computed from the integrated electron densities within these basins. These BECs were then used to estimate the valence states of each atomic species. This workflow provided quantitative data on atomic charge distribution, enabling comparison across different doped and non-stoichiometric configurations.

N. DFT+SPM Hybrid Approach

For the SPM-based calculation of CFPs, we extracted the required local structural data—namely, the Gd–O bond lengths and O–Gd–O angular coordinates—from DFT-optimized geometries (Table CI) and our previous structural work [70]. Intrinsic parameters $\bar{A}_k$ ($k = 2, 4, 6$) were adopted from studies on structurally analogous GdO_{12} clusters in tetragonal $SrTiO_3$ and $BaTiO_3$, using the reported values in cm^{-1}: $(\bar{A}_2, \bar{A}_4, \bar{A}_6) = (452, 156, 10)$ and $(470, 140, 8)$, respectively [30, 74]. Power-law exponents were set as $t_2 = 5$, $t_4 = 6$, and $t_6 = 10$, with the reference distance R_0 defined as the average Gd–O bond length within the coordination shell. To evaluate the sensitivity of the computed CFPs, we considered three models, hereafter referred to as model (a), model (b), and model (c): (a) employing nominal values from Ref. [30], (b) varying each intrinsic parameter $\bar{A}_k$ by ±20%, and (c) modifying the power-law exponents t_k by ±20%. This computational framework facilitated a parameter-space exploration necessary for validating the robustness and transferability of the derived CFPs across related compositions.

O. DFT+CFT Hybrid Approach

Central to our investigation is the accurate determination of crystal field parameters (CFPs) for Gd^{3+} in $PbTiO_3$, achieved through a dedicated hybrid DFT+CFT strategy integrating electronic structure and ligand field theories. To complement the DFT-based analysis and extract the CFPs associated with the localized $4f$ states of Gd^{3+} ions, we employed a post-processing methodology combining DFT and CFT (DFT+CFT). This approach enables a quantitative description of the electrostatic crystal field effects in a ligand environment, critical for rare-earth-doped perovskites. Starting from the self-consistent DFT calculations described above, we performed non-spin-polarized open-core simulations in which the Gd $4f$ electrons were treated as part of the ionic core. This initial step was necessary to isolate the electrostatic crystal field contributions before accounting for hybridization. The resulting electronic potentials were used to construct an effective Hamiltonian for the $4f$ orbitals. Hy-

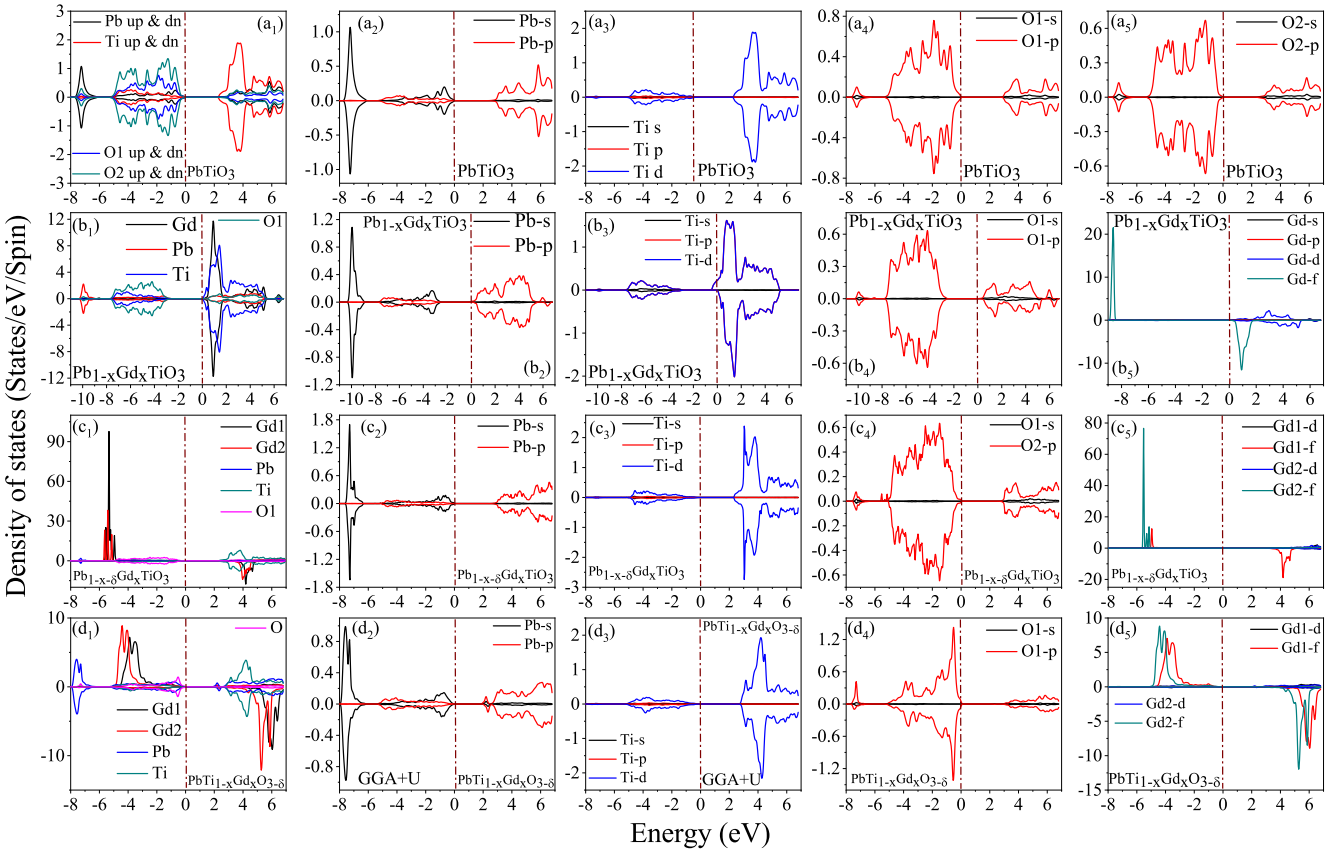

FIG. SM2. Spin-resolved projected density of states (PDOS) for pristine and Gd-doped $PbTiO_3$ systems calculated within GGA+U. Panels include orbital-resolved contributions from Pb (6s, 6p), Ti (3d), O (2p), and Gd (4f, 5d) states for (a_1–a_5) pristine $PbTiO_3$, (b_1–b_5) $Pb_{1-x}Gd_xTiO_3$, (c_1–c_5) $Pb_{1-x-\delta}Gd_xTiO_3$, and (d_1–d_5) $PbTi_{1-x}Gd_xO_{3-\delta}$. The Fermi level is set to 0 eV (vertical dashed line). These data provide detailed insight into orbital hybridization, Gd 4f localization, and defect-induced spin polarization that underpin the total DOS trends discussed in the main text.

bridization effects between the localized Gd 4f states and the O 2p valence orbitals were subsequently introduced through a semi-empirical correction characterized by the hybridization energy parameter Δ, as formulated by Novák *et al.* [7]. At this stage, the 4f electrons were reintroduced into the valence manifold and treated explicitly in a non-self-consistent calculation. This allowed us to capture the effects of covalency and electronic screening on the crystal field interaction without the computational overhead of full iterative convergence. The next step involved transforming the Bloch states to a localized Wannier representation using the Wannier90 package [14, 15]. This facilitated the projection of the local 4f Hamiltonian onto a compact orbital basis suitable for spherical tensor analysis. The CFPs were then extracted by expanding the local Hamiltonian in terms of Wybourne-normalized spherical tensor operators, enabling direct comparison with experimental spectroscopic data and multiplet structure predictions. All CFP calculations were carried out using the modified LANTHANIDE code described by Novák [7], which builds upon the foundational work of Edvardsson and Sondell [75]. Given the relatively weak material dependence of the radial integrals in the hybridization Hamiltonian H_A, we adopted average values for Gd^{3+} ions as tabulated in a comprehensive survey of optical data [31] and employed in subsequent studies such as [76]. This generalization improves the transferability of our results across a range of Gd-doped perovskite systems. By adopting this hybrid DFT+CFT strategy, we bridge the gap between *ab initio* electronic structure theory and phenomenological crystal field models, offering an internally consistent framework for interpreting the role of crystal symmetry and covalency in shaping the 4f level structure of lanthanide ions in complex oxides.

P. Zeeman Tensor and Susceptibility Evaluation via Hybridized Crystal Field Approaches

To estimate the components of the effective Zeeman g tensor and Van Vleck susceptibility tensor, we applied quadratic regression to the energy-level splittings derived using both the DFT+CFT and SPM+CFT approaches. In these calculations, the hybridization between the Gd 4f states and the O 2p/2s orbitals was enabled with a hybridization parameter $\Delta = -0.6$ Ry. The resulting computational workflows are denoted as "DFT+CFT+Δ+Zeem.+Reg." and "SPM+CFT+Zeem.+Reg.", respectively, and are used consis-

tently for evaluating magnetic anisotropies and paramagnetic responses.

SMIII. ORBITAL-RESOLVED ORIGIN OF GAP REOPENING AND LOCALIZED MAGNETISM

Figure SM2 provides the microscopic, orbital-resolved explanation for the total DOS trends discussed in the main text. By resolving contributions from Pb $6s/6p$, Ti $3d$, O $2p$, and Gd $4f/5d$ states, the PDOS clarifies how correlation, hybridization, and defect-induced symmetry lowering shape the electronic structure.

For pristine $PbTiO_3$, the valence band is dominated by O $2p$ states hybridized with Pb $6s$ and Ti $3d$, while the conduction band is primarily Ti $3d$ in character. The inclusion of U enhances Ti $3d$ localization and increases the band gap, consistent with correlation effects in transition-metal oxides.

In uncompensated $Pb_{1-x}Gd_xTiO_3$, highly localized and spin-polarized Gd $4f$ states cross E_F, directly accounting for the metallic behavior observed in Fig. 2(b) in the main article. Induced spin polarization in Ti $3d$ and O $2p$ states indicates finite exchange coupling between Gd moments and the host lattice.

In vacancy-stabilized systems, the Gd $4f$ states are displaced away from E_F, explaining the gap reopening in Figs. 2(c,d). Pb and O vacancies reduce local symmetry and modify orbital hybridization, leading to site-dependent PDOS features and enhanced spin polarization of O $2p$ states. These orbital fingerprints demonstrate how intrinsic defects simultaneously stabilize insulation and localized magnetism.

Thus, Fig. SM2 complements the main-text DOS by revealing the orbital-level mechanisms through which vacancy engineering enables insulating, spin-polarized states in Gd-doped $PbTiO_3$.

[1] S. Hüfner, *Optical Spectra of Transparent Rare Earth Compounds Academic*, Vol. 147 (1978).

[2] A. Abragam and B. Bleaney, *Electron Paramagnetic Resonance of Transition Ions*, International series of monographs on physics (Clarendon Press, 1970).

[3] B. Wybourne, *Spectroscopic Properties of Rare Earths* (Interscience Publishers, 1965).

[4] C. Rudowicz, Transformation relations for the conventional okq and normalised o'kq stevens operator equivalents with $k = 1$ to 6 and $-k \leq q \leq k$, J. Phys. C: Solid State Phys. **18**, 1415 (1985).

[5] C. Rudowicz and M. Karbowiak, Disentangling intricate web of interrelated notions at the interface between the physical (crystal field) Hamiltonians and the effective (spin) Hamiltonians, Coord. Chem. Rev. **287**, 28 (2015).

[6] L. Mollabashi and S. Jalali-Asadabadi, Crystal fields of lithium rare-earth tetrafluorides and multiplet splitting of the +3 rare-earth ions, Phys. Rev. B **102**, 045120 (2020).

[7] P. Novák, K. Knížek, and J. Kuneš, Crystal field parameters with wannier functions: Application to rare-earth aluminates, Phys. Rev. B **87**, 205139 (2013).

[8] L. Mollabashi, E. Sadeghi Kelishadi, and S. Jalali-Asadabadi, Crystal field and Ce^{3+} ion energy levels of $CeCl_3$ compound, Iran. J. Phys. Res. **18**, 105 (2019).

[9] L. Mollabashi, S. Jalali-Asadabadi, C. Rudowicz, M. Acikgoz, Z. Ghasemi-Dorcheh, R. Ebrahimi-Jaberi, M. Jalali-Asadabadi, S. Rahimi, and F. Jalali-Asadabadi, Numerical study of the temperature-dependent magnetization and susceptibility of Tm^{3+} in $LiTmF_4$, Phys. Rev. B **110**, 054440 (2024).

[10] S. J. Asadabadi, S. Cottenier, H. Akbarzadeh, R. Saki, and M. Rots, Valency of rare earths in $r\text{in}_3$ and $r\text{sn}_3$: ab initio analysis of electric-field gradients, Phys. Rev. B **66**, 195103 (2002).

[11] S. Asadabadi and H. Akbarzadeh, Density functional approach to study structural properties and electric field gradients in rare earth materials, Physica B **349**, 76 (2004).

[12] S. Jalali Asadabadi, Electronic structure and electric-field gradient analysis in Cein_3, Phys. Rev. B **75**, 205130 (2007).

[13] J. Kuneš, R. Arita, P. Wissgott, A. Toschi, H. Ikeda, and K. Held, Wien2wannier: From linearized augmented plane waves to maximally localized wannier functions, Comput. Phys. Commun. **181**, 1888 (2010).

[14] A. A. Mostofi, J. R. Yates, Y.-S. Lee, I. Souza, D. Vanderbilt, and N. Marzari, wannier90: A tool for obtaining maximally-localised wannier functions, Comput. Phys. Commun. **178**, 685 (2008).

[15] A. A. Mostofi, J. R. Yates, G. Pizzi, Y.-S. Lee, I. Souza, D. Vanderbilt, and N. Marzari, An updated version of wannier90: A tool for obtaining maximally-localised wannier functions, Comput. Phys. Commun. **185**, 2309 (2014).

[16] N. Marzari and D. Vanderbilt, Maximally localized generalized wannier functions for composite energy bands, Phys. Rev. B **56**, 12847 (1997).

[17] I. Souza, N. Marzari, and D. Vanderbilt, Maximally localized wannier functions for entangled energy bands, Phys. Rev. B **65**, 035109 (2001).

[18] D. Newman and W. Urban, Interpretation of s-state ion e.p.r. spectra, Adv. Phys. **24**, 793 (1975), https://doi.org/10.1080/00018737500101511.

[19] D. Newman and B. Ng, The superposition model of crystal fields, Reports on Progress in Physics **52**, 699 (1989).

[20] D. J. Newman and B. Ng, eds., *Crystal Field Handbook* (Cambridge University Press, Cambridge, 2000).

[21] M. Andrut, M. Wildner, and C. Z. Rudowicz, Optical absorption spectroscopy in geosciences: Part II: Quantitative aspects of crystal fields, in *Spectroscopic methods in mineralogy* (Mineralogical Society of Great Britain and Ireland, 2004).

[22] C. Rudowicz, P. Gnutek, and M. Açikgöz, Superposition model in electron magnetic resonance spectroscopy – a primer for experimentalists with illustrative applications and literature database, Appl. Spectrosc. Rev. **54**, 673 (2019), https://doi.org/10.1080/05704928.2018.1494601.

[23] K. W. H. Stevens, Matrix elements and operator equivalents connected with the magnetic properties of rare earth ions, Proc. Phys. Soc., Sect. A **65**, 209 (1952).

[24] M. Hutchings, Point-charge calculations of energy levels of magnetic ions in crystalline electric fields**this work was supported by the u.s. air force, the u.k. department of and industrial research, and the u.s. atomic energy commission (Academic Press, 1964) pp. 227 – 273.

[25] J. Jensen and A. Mackintosh, *Rare earth magnetism: structures*

and excitations, International series of monographs on physics (Clarendon Press, 1991).
[26] J. Mulak and Z. Gajek, *The effective crystal field potential* (Elsevier, New York, 2000).
[27] Y. Wan-Lun and Z. Min-Guang, Spin-hamiltonian parameters of ^{6}state ions, Phys. Rev. B **37**, 9254 (1988).
[28] M. Açıkgöz, R. Kripal, M. G. Misra, A. K. Yadav, P. Gnutek, and C. Rudowicz, Theoretical analysis of crystal field parameters and zero field splitting parameters for mn2+ ions in tetramethylammonium tetrachlorozincate (tmatc-zn), Polyhedron **235**, 116341 (2023).
[29] A. Biswas, S. Sarkar, Y. M. Jana, D. Swarnakar, S. Nandi, C. Rudowicz, M. Açıkgöz, and N. M. Avram, Analysis of crystal-field effect on luminescence spectra of Mn^{4+} ($3d^3$) ion-doped double perovskite La_2ZnTiO_6 phosphor by semiempirical computations: exchange charge model and superposition model, J. Mater. Chem. C **10**, 4355 (2022).
[30] W.-Q. Yang and W.-C. Zheng, Spin-hamiltonian parameters of Gd^{3+} ion in the room temperature tetragonal phase of $BaTiO_3$, Zeitschrift für Naturforschung A **69**, 606 (2014).
[31] C. Görller-Walrand and K. Binnemans, Optical spectroscopy and electronic structure of rare-earth ions in crystals, in *Handbook on the Physics and Chemistry of Rare Earth*, Vol. 23, edited by K. Gschneidner Jr and L. Eyring (North-Holland, Amsterdam, 1996).
[32] F. Tran and P. Blaha, Accurate band gaps of semiconductors and insulators with a semilocal exchange-correlation potential, Phys. Rev. Lett. **102**, 226401 (2009).
[33] D. Koller, F. Tran, and P. Blaha, Merits and limits of the modified Becke-Johnson exchange potential, Phys. Rev. B **83**, 195134 (2011).
[34] M. Yazdanmehr, S. J. Asadabadi, A. Nourmohammadi, M. Ghasemzadeh, and M. Rezvanian, Electronic structure and bandgap of Al_2O_3 compound using mBJ exchange potential, Nanoscale Res. Lett. **7**, 1 (2012).
[35] S. Jalali-Asadabadi, E. Ghasemikhah, T. Ouahrani, B. Nourozi, M. Bayat-Bayatani, S. Javanbakht, H. A. R. Aliabad, I. Ahmad, J. Nematollahi, and M. Yazdani-Kachoei, Electronic structure of crystalline buckyballs: fcc-C_{60}, J. Electron. Mater. **45**, 339 (2016).
[36] M. Yazdanmehr, S. Jalali-Asadabadi, J. Nematollahi, A. Nourmohammadi, and I. Ahmad, Predictions of bandgap and subbands of $\gamma - Al_2O_3$ in presence of intrinsic point defects by DFT+TB-mBJ, Comput. Condens. Matter **19**, e00379 (2019).
[37] G. Rehman, M. Shafiq, Saifullah, R. Ahmad, S. Jalali-Asadabadi, M. Maqbool, I. Khan, H. Rahnamaye-Aliabad, and I. Ahmad, Electronic band structures of the highly desirable iii–v semiconductors: TB-mBJ DFT Studies, J. Electron. Mater. **45**, 3314 (2016).
[38] D. Koller, F. Tran, and P. Blaha, Merits and limits of the modified Becke-Johnson exchange potential, Phys. Rev. B **83**, 195134 (2011).
[39] R. A. Jishi, O. B. Ta, and A. A. Sharif, Modeling of lead halide perovskites for photovoltaic applications, J. Phys. Chem. C **118**, 28344 (2014).
[40] J. Tauc, R. Grigorovici, and A. Vancu, Optical properties and electronic structure of amorphous germanium, Phys. Status Solidi B **15**, 627 (1966).
[41] S. Rahimi, R. Ebrahimi-Jaberi, F. Jalali-Asadabadi, L. Mollabashi, and S. Jalali-Asadabadi, Influence of (Ba,F) multidoping on structural, magnetic, optical, and electrical properties as well as performance enhancement of multiferroic $BiFeO_3$, Phys. Rev. B **106**, 115205 (2022).
[42] R. F. W. Bader, A quantum theory of molecular structure and its applications, Chem. Rev. **91**, 893 (1991).
[43] R. F. W. Bader, *Atoms in Molecules: A Quantum Theory (International Series of Monographs on Chemistry)* (Oxford University Press, 1994).
[44] E. Sjöstedt, L. Nordström, and D. Singh, An alternative way of linearizing the augmented plane-wave method, Solid State Commun. **114**, 15 (2000).
[45] G. K. Madsen, P. Blaha, K. Schwarz, E. Sjöstedt, and L. Nordström, Efficient linearization of the augmented plane-wave method, Phys. Rev. B **64**, 195134 (2001).
[46] K. Schwarz and P. Blaha, Solid state calculations using wien2k, Comput. Mater. Sci. **28**, 259 (2003), proceedings of the Symposium on Software Development for Process and Materials Design.
[47] P. Blaha, K. Schwarz, F. Tran, R. Laskowski, G. K. H. Madsen, and L. D. Marks, Wien2k: An APW+lo program for calculating the properties of solids, J. Chem. Phys. **152**, 074101 (2020), https://doi.org/10.1063/1.5143061.
[48] P. Blaha, K. Schwarz, G. K. Madsen, D. Kvasnicka, J. Luitz, R. Laskowski, F. Tran, and L. D. Marks, WIEN2k, in *An Augmented Plane Wave + Local Orbitals Program for Calculating Crystal Properties*, edited by Prof. Dr. Karlheinz Schwarz (Vienna University of Technology, Institute of Materials Chemistry, Getreidemarkt 9/165-TC, A-1060 Vienna, Austria, 2023).
[49] A. O. de-la Roza, M. Blanco, A. M. Pendás, and V. Luaña, Critic: a new program for the topological analysis of solid-state electron densities, Comput. Phys. Commun. **180**, 157 (2009).
[50] A. O. de-la Roza, E. R. Johnson, and V. Luaña, Critic2: A program for real-space analysis of quantum chemical interactions in solids, Comput. Phys. Commun. **185**, 1007 (2014).
[51] M. Yazdani-Kachoei and S. Jalali-Asadabadi, Topological analysis of electron density in half-heusler ZrXBi (M = Co, Rh) compounds: A density functional theory study accompanied by bader's quantum theory of atoms in molecules, J. Alloys Compd. **828**, 154287 (2020).
[52] M. Yazdani-Kachoei, S. Jalali-Asadabadi, and N. Arianmehr, Topological analysis of $CeMIn_5$ (M = Co, Rh) electron charge densities, Comput. Mater. Sci. **164**, 205 (2019).
[53] M. Berry, Classical adiabatic angles and quantal adiabatic phase, J. Phys. A: Math. Gen. **18**, 15 (1985).
[54] D. Vanderbilt, Berry-phase theory of proper piezoelectric response, J. Phys. Chem. Solids **61**, 147 (2000).
[55] M. V. Berry, Quantal phase factors accompanying adiabatic changes, Proc. R. Soc. London, Ser. A **392**, 45 (1984), https://royalsocietypublishing.org/doi/pdf/10.1098/rspa.1984.0023.
[56] D. Xiao, M.-C. Chang, and Q. Niu, Berry phase effects on electronic properties, Rev. Mod. Phys. **82**, 1959 (2010).
[57] S. Ahmed, J. Kivinen, B. Zaporzan, L. Curiel, S. Pichardo, and O. Rubel, Berrypi: A software for studying polarization of crystalline solids with WIEN2k density functional all-electron package, Comput. Phys. Commun. **184**, 647 (2013).
[58] V. I. Anisimov, J. Zaanen, and O. K. Andersen, Band theory and mott insulators: Hubbard U instead of Stoner I, Phys. Rev. B **44**, 943 (1991).
[59] V. I. Anisimov, F. Aryasetiawan, and A. I. Lichtenstein, First-principles calculations of the electronic structure and spectra of strongly correlated systems: the LDA + U method, J. Phys.: Condens. Matter **9**, 767 (1997).
[60] S. Rahimi, S. Jalali-Asadabadi, P. Blaha, and F. Jalali-Asadabadi, Nonzero spontaneous electric polarization in metals: novel predictive methods and applications, Sci. Rep. **14**, 672 (2024).
[61] F. Ge, W. Wu, X. Wang, H. Wang, Y. Dai, H. Wang, and J. Shen, The first-principle calculation of structures and defect energies in tetragonal $PbTiO_3$, Physica B **404**, 3814 (2009).

[62] S. Piskunov, E. Heifets, R. Eglitis, and G. Borstel, Bulk properties and electronic structure of $SrTiO_3$, $BaTiO_3$, $PbTiO_3$ perovskites: an ab initio hf/dft study, Comput. Mater. Sci. **29**, 165 (2004).

[63] C. H. Peng, J.-F. Chang, and S. B. Desu, Optical properties of PZT, PLZT, and PNZT thin films, MRS Online Proceedings Library (OPL) **243**, 21 (1991).

[64] R. T. R. Thomas and D. C. D. D. C. Dube, Structural, electrical and optical properties of sol–gel processed lead titanate thin films, Jpn. J. Appl. Phys. **36**, 7337 (1997).

[65] V. Železný, D. Chvostová, D. Šimek, F. Máca, J. Mašek, N. Setter, and Y. H. Huang, The variation of $PbTiO_3$ bandgap at ferroelectric phase transition, J. Phys.: Condens. Matter **28**, 025501 (2015).

[66] M. Gerges, M. Mostafa, and G. M. Rashwan, Structural, optical and electrical properties of $PbTiO_3$ nanoparticles prepared by sol-gel method, Ijlret **2**, 42 (2016).

[67] L. Bjaalie, A. Verma, B. Himmetoglu, A. Janotti, S. Raghavan, V. Protasenko, E. Steenbergen, D. Jena, S. Stemmer, and C. G. Van de Walle, Determination of the mott-hubbard gap in gdtio 3, Phys. Rev. B **92**, 085111 (2015).

[68] T. Shimada, T. Xu, Y. Araki, J. Wang, and T. Kitamura, Multiferroic dislocations in ferroelectric $PbTiO_3$, Nano Lett. **17**, 2674 (2017), PMID: 28291945.

[69] R. Ebrahimi-Jaberi and S. Jalali-Asadabadi, Elasticity and stability of gdal2 under pressure and temperature investigated using DFT+AI, Sci. Rep. **15**, 15573 (2025).

[70] M. Acikgoz, L. Mollabashi, S. Rahimi, S. Jalali-Asadabadi, and C. Rudowicz, DFT computations combined with semiempirical modeling of variations with temperature of spectroscopic and magnetic properties of Gd^{3+}-doped $PbTiO_3$, Phys. Chem. Chem. Phys. **25**, 3986 (2023).

[71] H. J. Monkhorst and J. D. Pack, Special points for brillouin-zone integrations, Phys. Rev. B **13**, 5188 (1976).

[72] T. Shimada, Y. Uratani, and T. Kitamura, Emergence of ferromagnetism at a vacancy on a non-magnetic ferroelectric $PbTiO_3$ surface: A first-principles study, Acta Mater. **60**, 6322 (2012).

[73] D. P. Dutta, B. P. Mandal, E. Abdelhamid, R. Naik, and A. K. Tyagi, Enhanced magneto-dielectric coupling in multiferroic Fe and Gd codoped $PbTiO_3$ nanorods synthesized via microwave assisted technique, Dalton Trans. **44**, 11388 (2015).

[74] W.-Q. Yang, W.-C. Zheng, and H.-G. Liu, Spin-hamiltonian parameters and local rotational order parameters for Gd^{3+} ion in the tetragonal phase of $SrTiO_3$ crystal, Physica B **406**, 3450 (2011).

[75] S. Edvardsson and D. Åberg, An atomic program for energy levels of equivalent electrons: lanthanides and actinides, Comput. Phys. Commun. **133**, 396 (2001).

[76] W.-Q. Yang, Y. Lin, W. Huang, and H.-Z. Zeng, Investigations of the spin-hamiltonian parameters and defect structures for Gd^{3+} ions in YMO_4 (M=V, P, As) crystals, Physica B **407**, 1268 (2012).